The SATIN Infrared Detector Development Program and the Road to HELLSTAR

Donald F. Figer[*a], Justin Gallagher[a], Lazar Buntic[a], Jonathan Getty[b], Stefan Lauxtermann[c]

[a]Rochester Institute of Technology, Center for Detectors, 74 Lomb Memorial Drive, Rochester, NY, 14623
[b]Raytheon Vision Systems, 75 Coromar Dr., Goleta, CA 93117
[c]Sensor Creations Inc., 5251 Verdugo Way, Suite I, Camarillo, CA 93012

ABSTRACT

We describe progress developing infrared detectors with HgCdTe grown on silicon substrates using Molecular Beam Epitaxial growth. The project is a collaboration between the RIT Center for Detectors and Raytheon Vision Systems (RVS). NASA and NSF jointly funded the program, known as SATIN (Short-wave infrared Advanced Technologies and Instrumentation program funded by NASA and NSF). We present detector characterization results for detectors made in the final lot of devices made by RVS. A full suite of characterization results, including for dark current, read noise, spectral response, persistence, linearity, full well, and crosstalk probability, are presented. The performance satisfies requirements for astronomy imaging applications. We plan to use the design to make HELLSTAR (HgCdTe Extremely Large Layout Sensor Technology for Astrophysics Research), a 4K×6K infrared detector with the highest number of pixels ever made for infrared astronomy.

Keywords: sensors, HgCdTe, infrared detectors, observational astronomy

*Donald F. Figer, E-mail: figer@cfd.rit.edu

1. INTRODUCTION

Infrared array detectors enabled scientific discovery since their inception in the 1980s, and they will likely continue to do so, such as for the James Webb Space Telescope (JWST) and future telescope projects. HgCdTe (MCT) is the material of choice for the most demanding infrared observations. It has excellent performance in the most relevant metrics and is versatile due to its tunable bandgap [1]. Detectors based on this material have widespread use in both ground-based and space-based astrophysics applications [2].

HgCdTe detectors have typically been grown on CdZnTe (CZT) substrates. While lattice spacing matches very well for the two materials, CZT wafers are expensive and usually small. In order to make larger and more affordable focal planes, the Center for Detectors (CfD) at the Rochester Institute of Technology (RIT) teamed with Raytheon Vision Systems (RVS) to develop hybrid infrared array detectors that use HgCdTe grown on silicon substrates. The initial roadblock in the development program was managing the effects of lattice mismatch between the materials [3] [4] [5] [6]. The most recent summary of this program is given in [7].

The development program is complete, and we now look forward to fabricating larger focal plane arrays, starting with HELLSTAR (HgCdTe Extremely Large Layout Sensor Technology for Astrophysics Research), a new 4K×6K×10 µm infrared detector with the highest pixel count ever made for astrophysics.

This paper presents the final results of the development program to make HgCdTe/Si infrared detectors. Section 2 describes the detector design implemented in the last fabrication run. Section 3 presents the characterization results of the HgCdTe/Si detectors from that run. Section 4 describes a new HELLSTAR detector development program and a related telescope application. Section 5 concludes with a summary and steps to produce the next generation of infrared detectors based on the development in this program.

2. THE SATIN DETECTOR DEVELOPMENT PROGRAM

The SATIN program (Short-wave infrared Advanced Technologies and Instrumentation program for NASA and NSF) developed near-infrared detectors through a series of design-fabrication-test iterations. RVS designed and fabricated the devices, while the CfD characterized them. Table 1 shows a summary of detectors fabricated and tested during the program. The table shows that not all tests have been done for every part. Rather, we selected specific tests for certain parts in order to diagnose inadequate performance and make changes in the design and fabrication recipes. All devices use the VIRGO multiplexer. Parts with "V" in their names have a range of parameter variations in the design of their unit cells. We used the characterization results from each phase of the project to make changes to the design for the next fabrication phase. After the last reported fabrication runs [7], RVS performed one final run to reduce anomalously-high read noise and extend the long-wavelength cutoff for an upcoming project at the South Pole. This run produced the hybrids designated as V21-V28.

Table 1. The table shows all the devices fabricated in the SATIN program, along with characteristics that we measured. The top two rows are for heritage devices that serve as a benchmark. The "V" parts have four variable unit cell (VUC) designs, one per quadrant. The "F" parts were designed and fabricated after testing the initial set of VUC parts. The final parts were also made in a VUC format.

Detector	Format	Cutt-off (µm)	substrate	Dark Current	Egain	Photon Transfer	Read Noise	Full Well	Linearity	Quantum Efficiency	Crosstalk	Persistence	Intrapixel Sensitivity
VIRGO-9A	2K x 2K	1.7	CZT	✔	✔	✔	✔	✔	✔	✔	✔	✔	✔
VIRGO-14	2K x 2K	2.5	Si	✔	✔	✔	✔	✔	✔	✔	✔	✔	
VIRGO-V1	1K x 1K	2.5	Si	✔	✔	✔				✔			
VIRGO-V2	1K x 1K	2.5	Si	✔	✔	✔				✔			
VIRGO-V4	1K x 1K	2.5	Si	✔	✔	✔				✔			
VIRGO-V5	1K x 1K	2.5	Si	✔	✔	✔				✔			
VIRGO-V6	1K x 1K	2.5	Si	✔	✔	✔				✔			
VIRGO-F3	1K x 1K	2.5	Si	✔	✔	✔	✔	✔	✔	✔	✔	✔	
VIRGO-F6	1K x 1K	2.5	Si	✔	✔	✔	✔	✔	✔	✔	✔	✔	✔
VIRGO-VTHIN1	1K x 1K	2.5	Si	✔	✔	✔		✔	✔	✔	✔	✔	
VIRGO-F7	1K x 1K	2.5	Si	✔	✔	✔	✔	✔	✔			✔	
VIRGO-F8	1K x 1K	2.5	Si	✔	✔	✔	✔	✔	✔			✔	
VIRGO-V7	1K x 1K	2.5	Si	✔	✔	✔	✔	✔	✔	✔	✔	✔	
VIRGO-F10	1K x 1K	2.5	Si	✔	✔	✔	✔	✔	✔	✔	✔	✔	
VIRGO-F13	1K x 1K	2.5	Si	✔	✔	✔	✔	✔	✔	✔	✔	✔	
VIRGO-F15	1K x 1K	2.5	Si										
VIRGO-V8	1K x 1K	2.5	Si										
VIRGO-F17	1K x 1K	2.5	Si	✔	✔	✔	✔	✔	✔	✔	✔	✔	
VIRGO-V21	1K x 1K	2.5	Si	✔	✔	✔	✔	✔	✔	✔	✔	✔	
VIRGO-V22	1K x 1K	2.5	Si	✔	✔	✔	✔	✔	✔	✔	✔	✔	
VIRGO-V23	1K x 1K	2.65	Si	✔	✔	✔	✔	✔	✔	✔	✔	✔	
VIRGO-V24	1K x 1K	2.65	Si	✔	✔	✔	✔	✔	✔	✔	✔	✔	
VIRGO-V25	1K x 1K	2.65	Si										
VIRGO-V28	1K x 1K	2.65	Si	✔	✔	✔	✔	✔	✔	✔	✔	✔	
V* are Variable Unit Cell (VUC) devices													
substrate removed devices in green													

From the final detector wafer fabrication lot run, RVS hybridized detector die from two MBE-grown HgCdTe layers with planar geometry on six inch silicon wafers on to VIRGO multiplexers. Although originally funded to fabricate only two hybridized detectors, Raytheon delivered six. Each has variable unit cell design per quadrant to optimize junction size, contact size, and implant parameters. The long wavelength cutoff for this last lot was designed to be extended by 0.15 µm, as compared to the cutoff for earlier devices, so that the detectors can serve as prototypes for a proposed project for a large focal plane to be deployed at the South Pole [8]. Figure 1 shows a picture of what is believed to be the best detector from the lot, VIRGO-V23.

Figure 1. The image shows the VIRGO-V23 detector on the left and the container lid on the right.

RVS designed the latest wafers with buffer layers that are much thicker than those in designs used for the previous runs with the expectation that this would reduce the large tails seen in the distributions of the dark current. In addition to thicker buffer layers, four combinations of annealing and substrate removal processes were applied to the two wafers to study the effects of different processes on the dark current and other performance metrics. The two wafers were subjected to different annealing processes, the nominal process used for earlier devices in the program and a newer alternative process. Two 1K×1K sensors from each wafer were, in turn, subjected to two different substrate removal processes, a baseline process and an alternative process. Four different combinations of annealing and substrate removal processes were applied to the four detectors produced in the latest fabrication round, as summarized in Table 2. The intent of this comparison was to develop the best recipes for future fabrication runs.

Table 2. The table shows a summary of parts and their processing used for the latest fabrication run. The color coding relates to defect density, where green is better than red.

Part number	Planning	Epoxy wick	Det wafer	Det die	ROIC wafer	ROIC die
First kit batch						
Satin-21	EWO_3339	Yes, wicked	5017314	D2	5014369	A3
Satin-22	EWO_3339	Yes, wicked	5017314	D4	5014369	A4
Satin-23	EWO_3339	Yes, wicked	5017315	D3	5014369	C3
Satin-24	EWO_3339	Yes, wicked	5017315	D5	5014369	C4
Second kit batch						
Satin-25	EWO_3332	Not wicked	5017315	D2	5014369	C6
Satin-26	EWO_3332	Not wicked	5017315	D4	5014369	D7
Satin-27	EWO_3332	Not wicked	5017315	E3	5014369	D2
Satin-28	EWO_3332	Not wicked	5017315	E4	5014369	D3

3. DETECTOR CHARACTERIZATION

We report characterization results in this section using experiments described in [7]. Unless otherwise stated, all results are for quadrant four (lower left) of V23, given that this quadrant and device yielded the best performance.

3.1 Linearity, Full Well, and Conversion Gain

We measure linearity and well depth by exposing the detector to a flat field of 1550 nm light for a fixed amount of time so that the detector saturates while still in range of the digitizing electronics. In practice, the photon transfer experiment acquires the data to generate the results. This experiment also produces conversion gain as a result. Figure 2. shows the results for well depth and linearity. The upper plot is a histogram of pixel values at the point when the detector is fully saturated. The bottom plot shows the implied flux divided by the actual flux. As expected, it shows that the apparent response becomes less as the pn junction of the well is filled at higher fluences. The equation in the legend is a polynomial fit to the nonlinearity, where only the filled symbols are used. At some point, ~435,000 e⁻, the detector becomes non-responsive, *i.e.*, it is saturated. The standard deviation of well depths is approximately 10,000 e⁻.
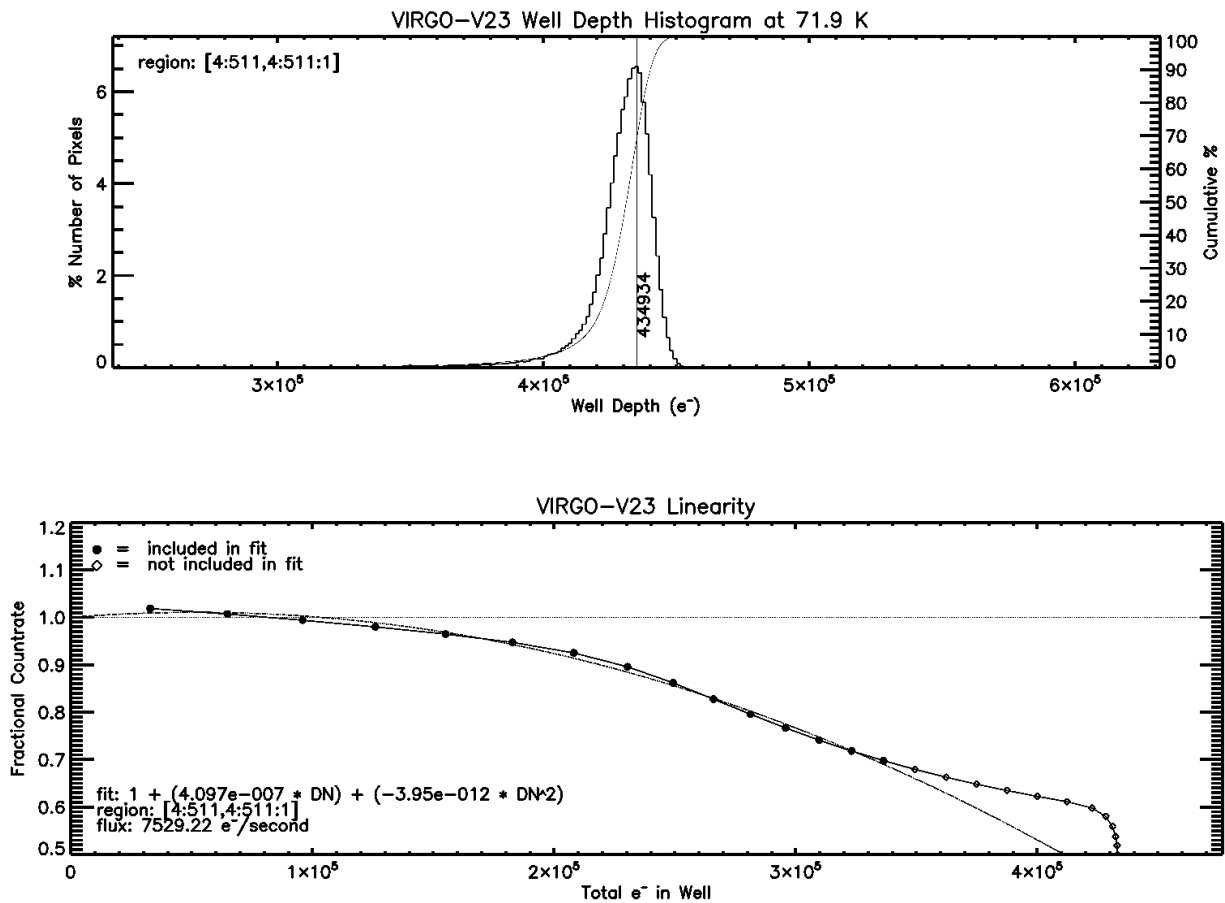
\\falcon\disk1\VIRGO-V23\cold1\JMCE\photon_xfer\photon_xfer.24Aug21\results\Q4\VIRGO-V23_linsat_e.jpg

Figure 2. The plots show well depth and linearity for quadrant four of V23. The upper plot shows a histogram of pixel values at the point of saturation. The average full well is ~435,000 e⁻. The lower plot shows the inferred flux divided by the actual flux. It starts at one, indicating that the detector has a linear response. With high fluence, the detector becomes nonlinear until it becomes unresponsive to additional light at the saturation point.

Figure 3 shows photon transfer plots for the same type of data used to generate the results in Figure 2. The panels in the figure are arranged in the same geometry as the quadrants on the array, *i.e.*, quadrant one is in the upper left and quadrant number increases clockwise. There is a line fit to the first five data points in each plot, and the inverse slope of that line is

4

the conversion gain. The conversion gain varies from a low of 11.85 e⁻/ADU in quadrant one (upper left) to a high of 12.95 e⁻/ADU in quadrant four (lower left). Note that the absolute numbers depend on the amplification in the post-detector electronics, which was two for the data in the figure. Conversion gain for other amplifications are consistent with these data compared to what would be expected.
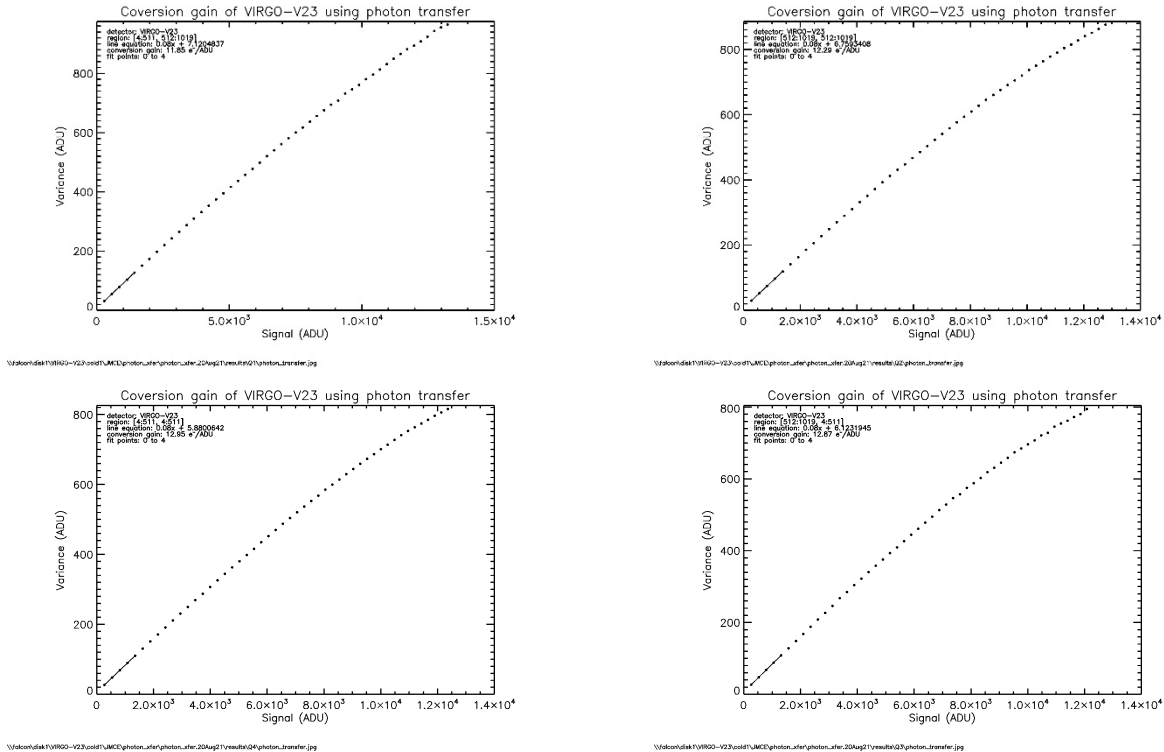
Figure 3. The plots show results of the photon transfer experiment for all four quadrants, where quadrant one in the upper left panel corresponds to the upper left quadrant of the array and the quadrants are numbered clockwise. In all cases, the data are well behaved and as expected. Variations in the conversion gain, shown in the legends, are due to variations in the pn junction geometry in the different quadrants, with the highest conversion gain for quadrant four. Note that only the first five data points are used to fit a line to the data so that the results are not impacted by the nonlinearity of the device that can be seen at higher fluence.

Another result from the photon transfer experiment is a flat field image. Figure 4 shows a flat field using 1550 nm light. One can clearly see the quadrant structure that would be expected given the variation in conversion gain shown in Figure 3. The units, shown in the scale on the right, are ADU. After removing data for pixels with anomalously high values, *i.e.* "hot pixels," we calculate a standard deviation of ~2-3% across the flat field in each quadrant. Note that the hot pixels were not corrected before making the image in the figure.

On close examination of the figure, one can see relatively dark pixels, in addition to the white hot pixels. The dark pixels have signals that are already near full well in the first read, as if they start integration at an anomalously-high offset with little well-capacity leftover to integrate signal. When isolated and corrected for nonlinearity, the signal of high-offset pixels increase with read number. This behavior is expected if these pixels integrate charge but are already near full well before the very first read is taken. The white hot pixels in the figure have signals that start at typical offset levels but increase with varying slope versus read number. The slope begins at a higher level than typical and then settles to a more typical value. The curve of signal versus time appears to be similar to that of voltage versus time for an "RC" circuit.

9.35e+003
8.27e+003
7.2e+003
6.13e+003
5.06e+003
3.98e+003
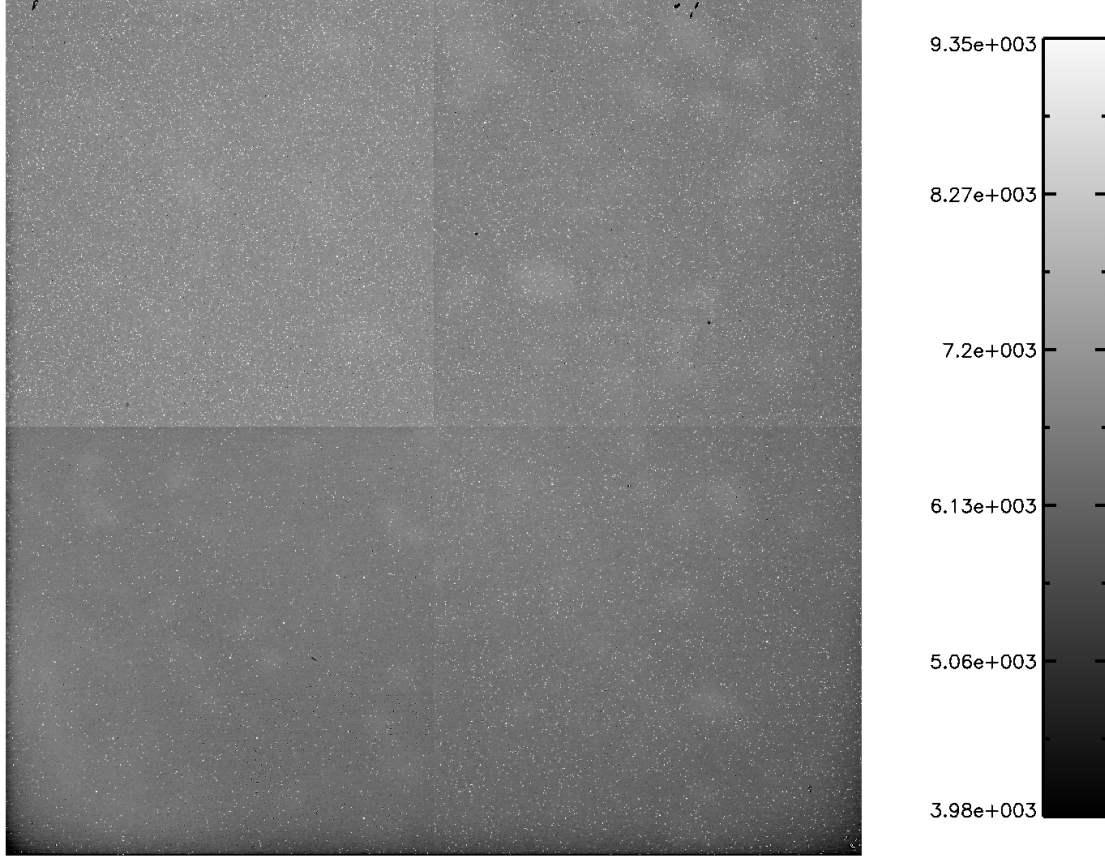
\\falcon\disk1\VIRGO−V23\cold1\JMCE\photon_xfer\photon_xfer.20Aug21\results\region1\maps\photon_xfer_70K_50_1_1550_19.fits25_0.jpg

Figure 4. The image shows the response to uniform illumination, *i.e.*, it is a "flat field."

Figure 5 shows an image taken with V23. The target is an opaque screen with small holes punched into it. It was exposed to collimated light, and a cryogenic J-band filter was in the beam. The image on the left is raw and the image on the right represents the data after calibration for bias structure, dark current, and flat-field response. Both images use the same scale. The faint circles around each pinhole image represent Airy rings. One can see complex interference patterns where neighboring rings intersect. Isolated dark and light pixels in the reduced image likely represent expected cosmic ray secondary hits in one of the source or calibration frames. The reduced image demonstrates that the detector produces the kind of images one would expect to see for point-like objects. The quadrant nature of the device is not apparent in the reduced image, testament to the quality of the calibration.
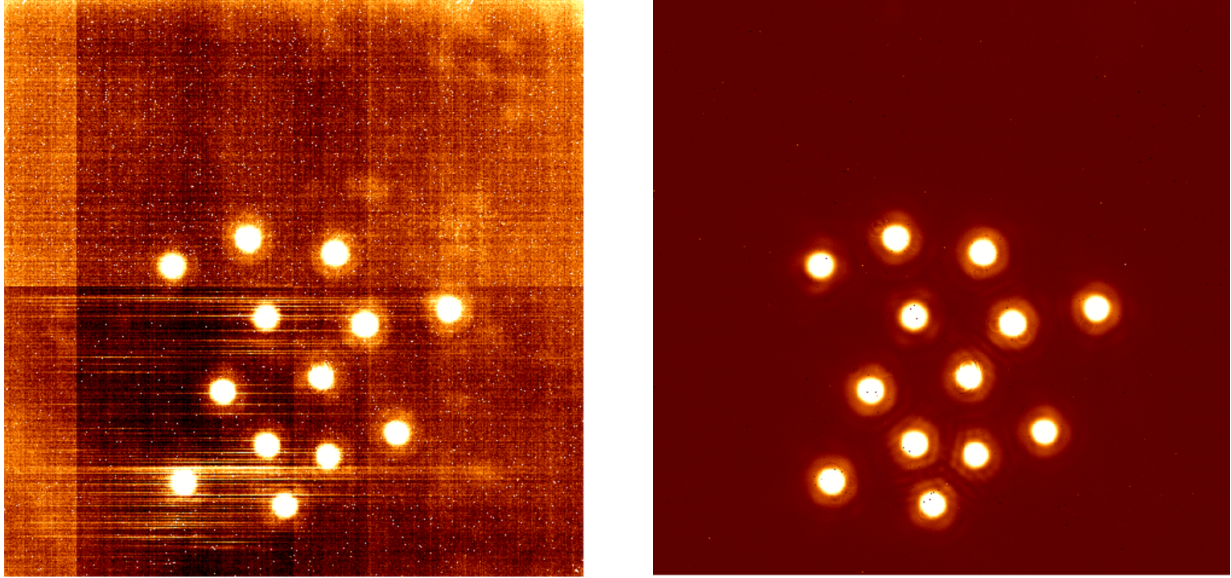
Figure 5. These are two images taken with V23. (left) This is a raw image of a target with multiple pinholes, illuminated by a collimated beam of light passing through a cryogenic J-band filter. (right) This is a reduced version of the image on the left. Bias structure and dark current have been subtracted. The image has been corrected for flat-field response.

3.2 Crosstalk

The crosstalk of V23 and F17, a predecessor device to V23, is similar with variation of a few tenths of a percent of the central pixel (Figure 6). The number of events in each case is high enough for the results to be reliable. Both parts are wicked, meaning that epoxy was inserted into the spaces between bump bonds to provide greater mechanical integrity. One problem with wicking is that interpixel capacitance is amplified by the increased dielectric constant of the epoxy as compared to the vacuum between bonds when epoxy is not used. The results in the figure show that wicked parts do not have very high crosstalk, and thus do not have high interpixel capacitance. They also suggest that the new planar geometry of the detector produces better performance in this metric compared to the previous mesa-style geometry used for F17.

detector temperature (K): 72.0
number of images: 18
number of events: 277
date: Sat Aug 21, 2021
region: [4:1019,4:1019]
crosstalk results (%):

−0.05	0.22	−0.03
0.20	100.00	0.34
−0.03	0.20	−0.01

detector temperature (K): 73.0
number of images: 40
number of events: 1768
date: Thu May 27, 2021
region: [4:1019,4:1019]
crosstalk results (%):

−0.11	0.32	−0.09
0.43	100.00	0.49
−0.12	0.34	−0.12

Figure 6. Crosstalk is similar for V23 (left) and F17 (right). The nearest-neighbor values are low for both devices, and somewhat lower for V23 as compared to F17.

3.3 Read Noise

Up until the final lot, all devices had high read noise that was atypical for infrared detectors using the VIRGO multiplexer. An example of this high read noise is shown in the left panel of

, where one can see correlated double sampling (CDS) read noise of approximately 60 e⁻ for part F13, a factor of three higher than typical. The thick solid line represents a reduction in read noise of one divided by the square root of the number

of sample pairs. The data can deviate from that curve at high sample number because those samples require more time to read, subjecting the data to greater integrated dark current and related shot noise. The right plot in the figure for V23 shows read noise that is at least a factor of two lower than for F13. The success in reducing the read noise in the final parts represents the final hurdle in advancing this technology toward making science grade detectors.
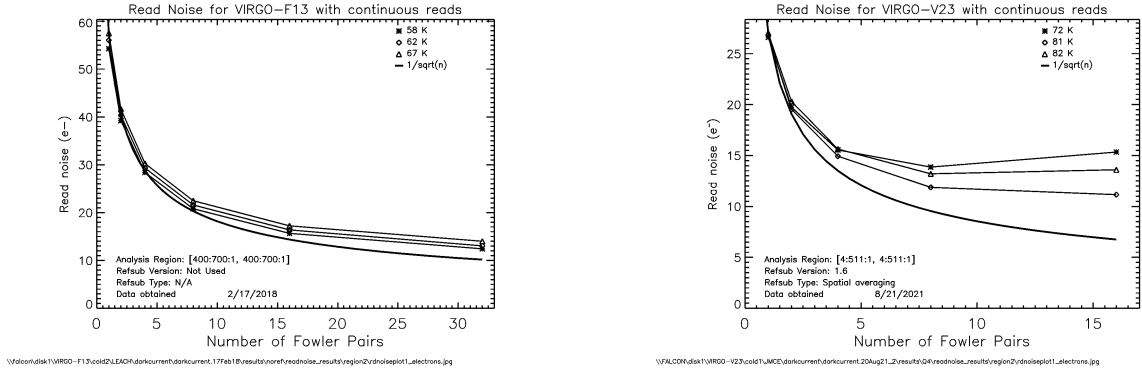

Figure 7. The read noise of VIRGO-F13 (left) vs. VIRGO-V23 (right) versus number of samples is in the upper panels. The problem of anomalously-high read noise in the F parts has been solved.

Another effect seen in all earlier devices is a strong relationship between CDS read noise a temperature (see Figure 8). The panel on the left shows strongly increasing read noise with higher temperature for F13. On the right, one can see that this effect has been removed in V23, where the read noise is constant with temperature, as is typical for infrared detectors using the VIRGO multiplexer. We take this as an indication that design changes made for the final parts were successful.
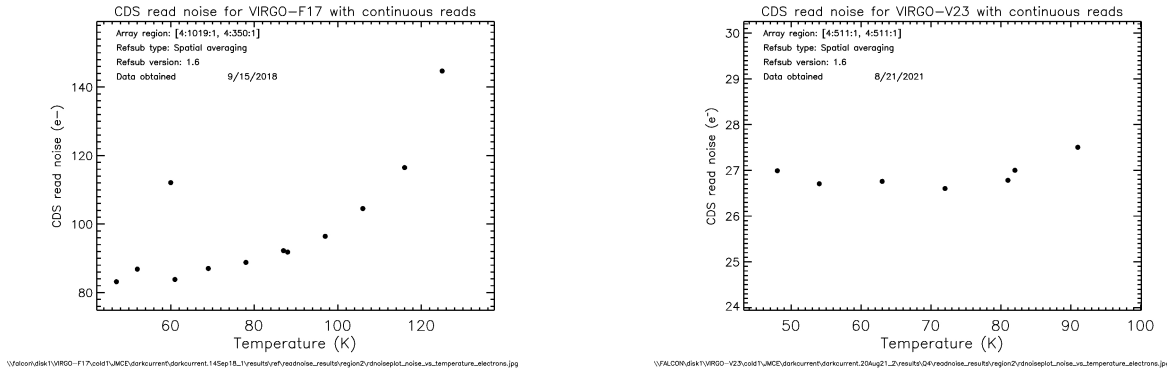
Figure 8. The plots show read noise versus temperature for VIRGO-F13 (left) vs. VIRGO-V23 (right). The problem of temperature-dependent read noise in the F parts has been solved in the latest parts.

We believe that this read noise problem was solved by using a planar architecture, instead of the typical mesa-style junctions of earlier devices. This assertion was supported by probe data obtained for test structures. Figure 9 compares open field of view probe data from three HgCdTe/Si test structures at a temperature of 77 K. The curves on the left are for devices made with the standard mesa-delineated structures. The forward bias region at I=0, highlighted in the blue circle, shows that the current does not increase with additional bias voltage, i.e. it is a non-Ohmic contact. The curves on the right show measurements from a p-type pocket-implanted planar structure. A fully Ohmic contact is achieved in the implanted structure by optimizing the implanted p-doping.
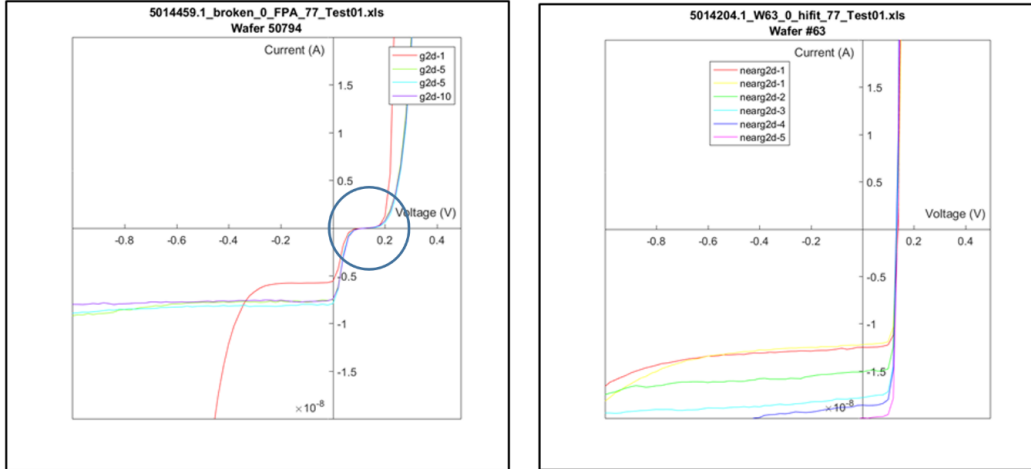
Figure 9. The curves show a comparison of I-V curves for Raytheon mesa-delineated devices (left), as used in the current project, and for an implanted planar structure device (right). Test was performed under full field of view at 77K.

3.4 Quantum Efficiency

Figure 10 shows that the quantum efficiency for V23 is high in the K-band and that the long wavelength cutoff has been successfully extended from 2.45 μm to 2.65 μm. The short wavelength cutoff is near 800 nm, as expected for parts that have their silicon substrates removed, but have not had their buffer layers completely removed. The apparent noisiness of the data is due to low flux and QE on the short wavelength end and high thermal background on the long wavelength end.
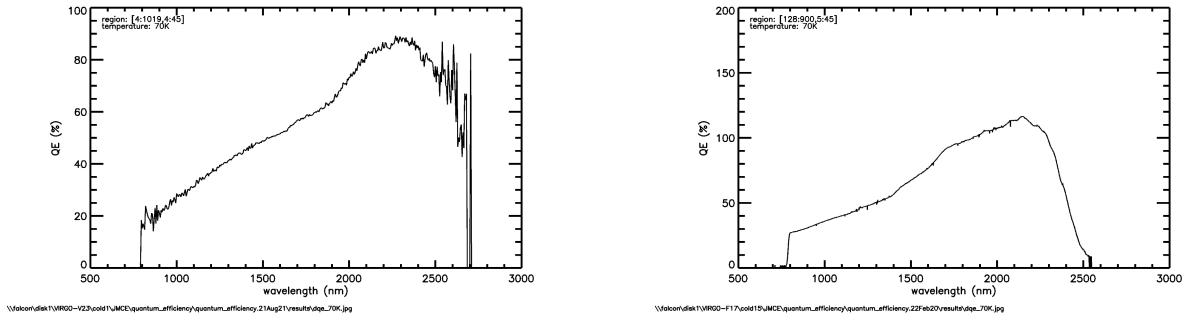
Figure 10. The panels show quantum efficiency for V23 (left) and F17 (right). Note the difference in vertical scale. The accuracy of the measurement is approximately 10%, as implied by the values above 100% in the plot on the right.

3.5 Persistence

To measure persistence, we take long exposure images in the dark after exposing the detector to a fixed photon fluence expressed as a fraction of the full well fluence. Devices from previous lot runs had persistence of approximately 1%.

In the new lot run, the persistence is a few tenths of a percent at high fluence. Figure 11 shows results for 25% and 75% full well. Data labels refer to wavelength in nanometers. If each liberated photon represents one trap, then the number of traps responsible for the persistence is approximately 100 per pixel. This low persistence is a significant achievement, given the higher persistence measured for parts from earlier lot runs.

VIRGO−V23 persistence versus fluence
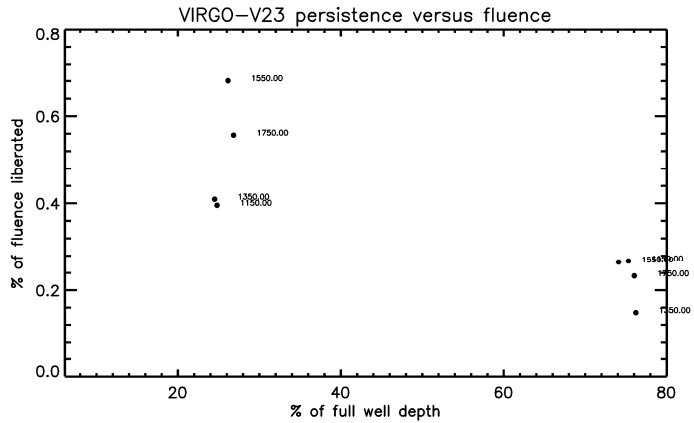
\\falcon\\disk1\VIRGO−V23\cold1\JMCE\persistence\persistence.22Aug21\results\Q4\persistence_vs_fluence_jumbo_VIRGO−V23.jpg

Figure 11. Persistence versus fluence is shown for V23 at 25% and 75% fluence.

3.6 Dark Current

Figure 12 shows dark current measurements. The levels are approximately a factor of 10 higher compared to F17, but still relatively low for broadband imaging applications. The constant level versus temperature implies that the measurements might be affected by blackbody radiation from the filter wheel or a light leak. We will explore these possibilities. The panel on the right of the figure shows the typical high dark current tail, albeit reduced as compared to parts made earlier in this program. We attempted a vacuum thermal anneal at 130 C, a process that reduced the tail for F17, in order to reduce the tail further. It yielded no change in the dark current behavior, a result that is not very surprising because the tail is already as small as the post-anneal tail for F17.
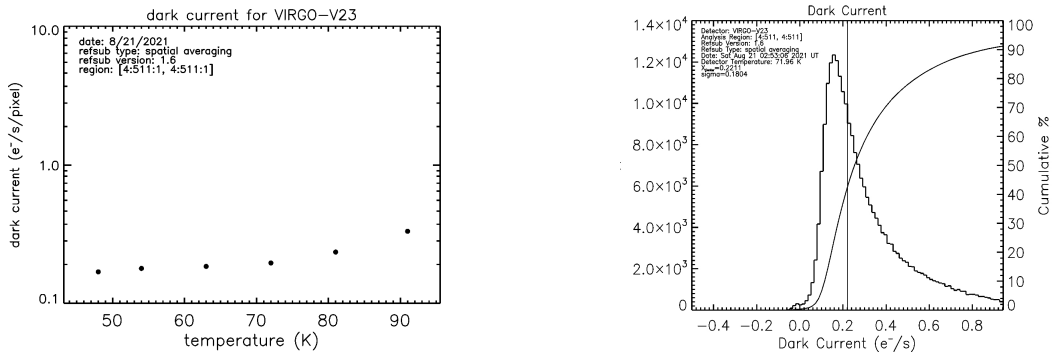
\\FALCON\disk1\VIRGO−V23\cold1\JMCE\darkcurrent\darkcurrent.20Aug21_2\results\Q4\slopeplots\region2\darkjumbo_versustemp_VIRGO−V23_a.jpg   \\FALCON\disk1\VIRGO−V23\cold1\JMCE\darkcurrent\darkcurrent.20Aug21_2\results\Q4\slopeplots\region2\histograms\dark_70K_893.127_utc_50_10_a

Figure 12. The plot shows dark current versus temperature for quadrant four of V23 (left). It is roughly constant over the range with an average of ~0.2 e$^-$/second/pixel. The dark current distribution has the typical shape seen for earlier parts, although the high dark current tail is smaller than for the first lot runs in the program (right).

Figure 13 is a dark current map for VIRGO-V23, where black is used for a value of 0 and white for 1 e$^-$/s/pixel. As can be seen, quadrant four (lower left) has the lowest dark current of all quadrants. The data were taken with the detector at a temperature of 70 K. The distribution of high dark current pixels appears to be random within quadrants, with the highest levels in the upper left quadrant and increasing clockwise. The lower dark current in quadrant four partially provides the motivation for using that quadrant in the bulk of this paper. It also suggests that the detector design for that quadrant should be favored in future designs.
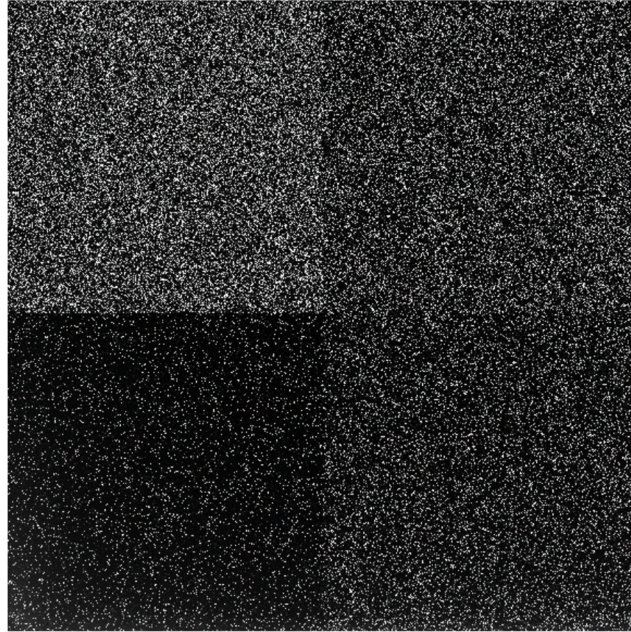
10

Figure 13. This is a dark current map for VIRGO-V23. The lower scale (black) is 0 and the upper (white) is 1 e⁻/s/pixel.

An exploration in the data reveals that pixels generally have behavior that can be described in three categories: linear, nonlinear, and linear with high initial offset (see Figure 14). The bottom row in the figure shows good pixels that exhibit linear behavior (green) and hot pixels that exhibit nonlinear behavior (red). The upper row shows 'high-offset' pixels, which start off at an abnormally high signal, but otherwise behave linearly (black). The pink lines correspond to pixels that reach saturation early (perhaps because they have a lower full-well depth) while the purple lines exhibit significant nonlinearity before returning to a linear mode of operation. The first two columns of plots were created using the same reference voltage, but different gains; hence the pixels in the middle column reaching saturation in earlier frames. The third column of plots was created with an increased reference voltage, resulting in a slight nonlinearity and quicker saturation.

We attempted to identify linear and nonlinear pixels by measuring the concavity of their signals versus time via the second derivative. Figure 15 shows two relevant plots. The first depicts the second derivative of pixel values through a series of 50 frames. The good pixels (green) behave linearly, and thus have a constant second derivative. Pixels that do not have linear behavior (red) produce curves in the second derivative plot. Taking the standard deviation of the second derivative (SDSD) has proven a simple and effective way to find the number of pixels that behave anomalously. The second plot shows the standard deviations of pixels in each quadrant, as well as the full array. Note that quadrant four has the smallest tail, implying that it has fewest hot/nonlinear pixels, which is consistent with the dark current map shown in Figure 13. Of the full array, 1.6% of the pixels have an SDSD>10. In quadrant four, only 0.8% of pixels have an SDSD>10, while nearly 2.6% of pixels in quadrant one exceed this limit.
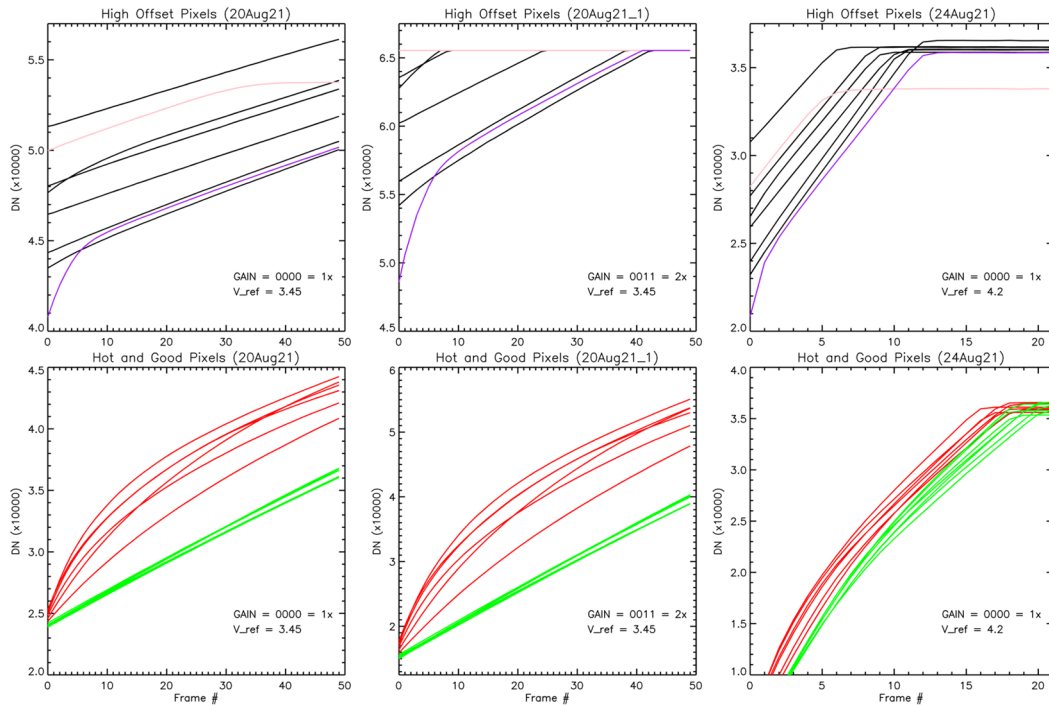
Figure 14. These plots show dark current plots for well behaved, linear pixels (green), hot pixels that exhibit nonlinear behavior (red), pixels that start at an abnormally high signal (black), high-offset pixels that saturate earlier than others (pink), and high-offset pixels that exhibit nonlinear behavior (purple.) Note the changes in electronic gain and reference voltage between columns of plots.
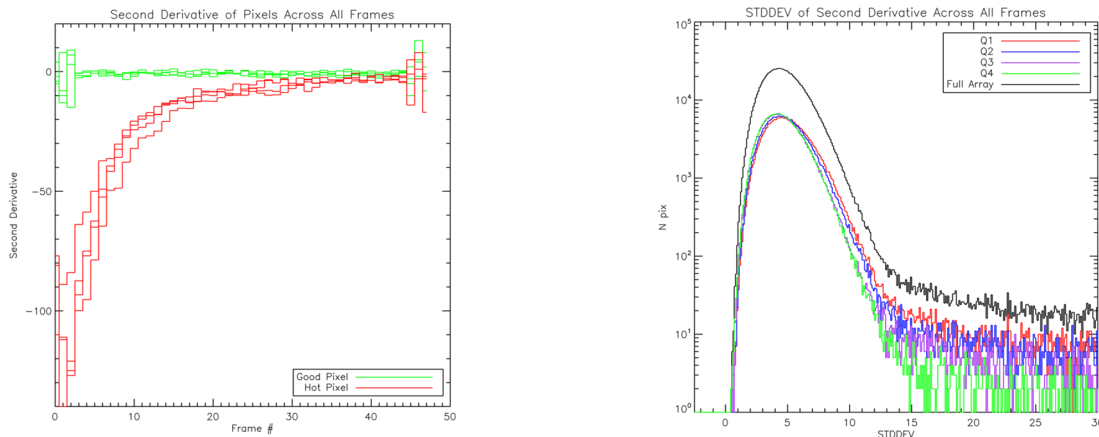

Figure 15. These plots show how we calculate the second derivative of the signal through a series of 50 frames for the V23 detector. Shown on the left are plots for a few good pixels (green), and hot pixels (red). Shown on the right are the standard deviations of pixel values in each quadrant; Note that the tail for quadrant four is lower than the other quadrants.

4. HELLSTAR

HELLSTAR is HgCdTe Extremely Large Layout Sensor Technology for Astrophysics Research, a new infrared detector design with the highest pixel count ever made for astrophysics. The design uses advances from the SATIN development program. HELLSTAR will have wide applicability to many astronomy projects, particularly for the target application of a large area infrared focal plane in a telescope at the South Pole.

The baseline design HELLSTAR uses MCT/Si hybridized to existing readout integrated circuit (ROIC) multiplexers designed by Sensor Creations, Inc. (SCI). The CfD and SCI, in collaboration with Roger Smith of Caltech and Murzy Jhabvala of NASA Goddard Spaceflight Center, developed a testing program to validate the operation of SCI's existing ROICs at the wafer level.

Figure 16 shows three images obtained with a ROIC die on a wafer while a laser light was projected onto it. They were obtained during the RIT/SCI testing program and show that the many circuits needed to obtain an image with the ROIC work. The light appears in inverse color scale as the elongated smear. In addition to this test, SCI had already separately validated many of the individual steps necessary to operate the device, such as row and column clocking and transmission of the pixel voltage through the pixel FET, the column FET, and the output FET. This testing program suggests that the yield to working die on a wafer is likely >10%. This is encouraging, given the complexity of the circuit and bodes well for the manufacturability of full hybrid focal planes.
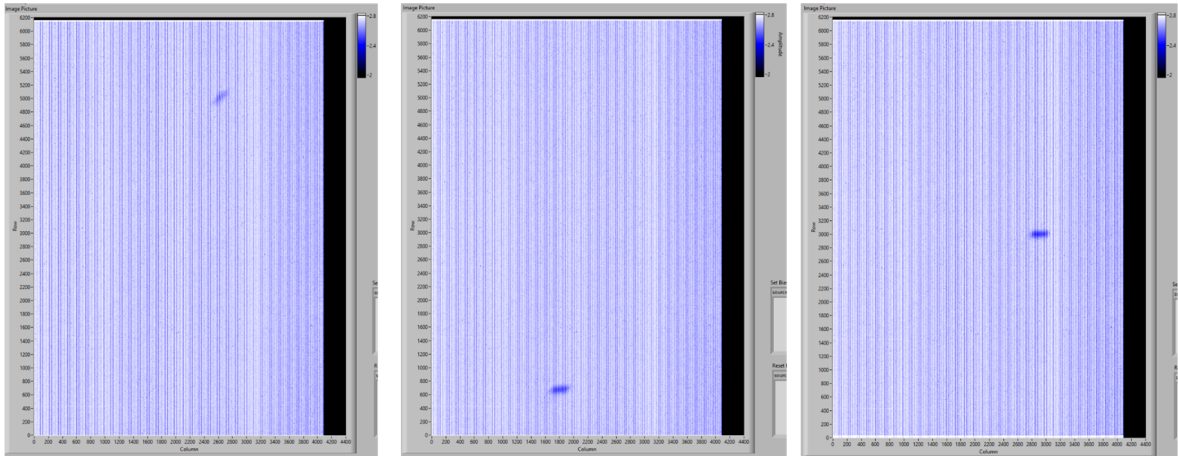

Figure 16. The pictures are screenshots of raw data displayed in a GUI and obtained by exposing one of the SCI 4K×6K ROICs to a red laser pointer (650 nm) and reading the pixels in 32-output mode. Photo-generated electrons are collected by the n-type implant of the NMOS reset transistor. The position of the laser pointer was moved in between the images and can be seen as the elongated dark smear.

Table 3 shows the performance of the SATIN detectors (*middle column*), compared to the requirements for HELLSTAR (*right column*), which are based on all the advances made in the SATIN program. In general, the requirements are more stringent than what is needed for most broad-band imaging applications.

Table 3. The table shows HELLSTAR goals compared to SATIN performance.

Parameter	SATIN Performance	HELLSTAR Goals
Format	1K×1K and 2K×2K	4K×6K
Pixel Size (μm)	20	10
Read Noise (e⁻ CDS)	27	20
Wavelength Range (μm)	0.8 – 2.55	0.8 – 2.65
Dark Current (e⁻/s/pixel)*	0.5 @ 70 (95% Operability)	0.1
Minimum readout time (s)	0.3	1
Well size (e⁻)	400,000	300,000
Peak QE (w/AR coating)	>90%	>70% in K-band
Persistence (after 100% saturation)	<0.1%	<0.1%

The first target application for HELLSTAR is the Cryoscope (PI Kasliwal), a proposed 1-m class telescope that would cover a wide field at infrared wavelengths and leverage the cold environment at the South Pole. The telescope would be very cold and deliver a low thermal background in the K-band. The focal plane would have 629 Mpixels in a 6×4 mosaic of 4K×6K×10 μm hybridized detectors. The focal plane will cover 49 deg^2 every 1000 seconds with SNR>5 for magnitude 23.3 at 2.3<λ<2.55 μm. The areal coverage in just one exposure is equivalent to the area that would be covered by a square measuring 14 full moons on a side, or about four times the areal coverage of the focal plane in the Large Synoptic Survey Telescope in the Vera Rubin Observatory. The design concept (see Figure 17) is being developed through a program funded by NSF (ATI Award #2010041, PI Roger Smith).
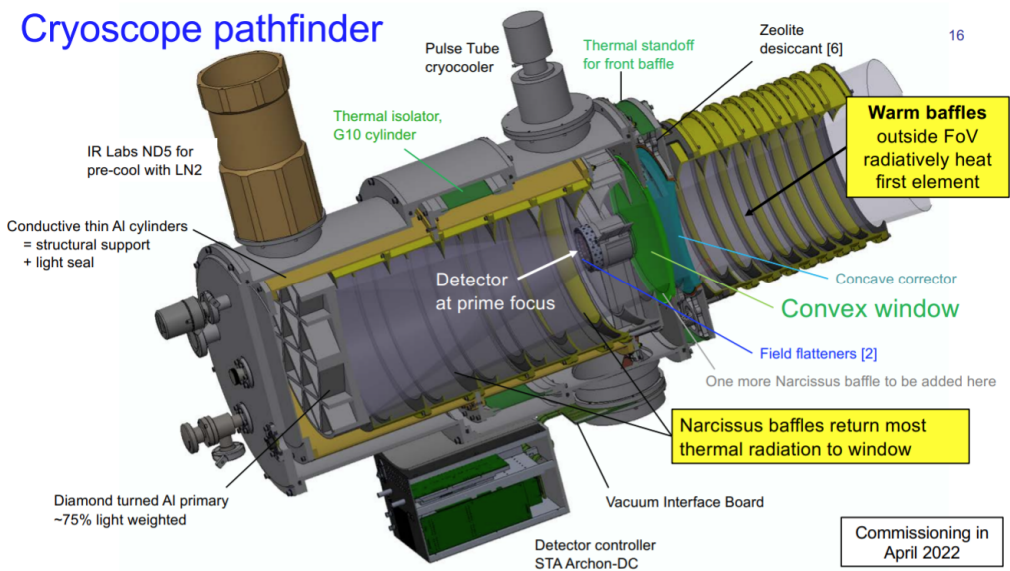

Figure 17. This solid model rendering shows a cutout of the Cryoscope pathfinder camera that Roger Smith is developing through NSF ATI funding.

With the parameters in Table 3, HELLSTAR would lead to background-limited-performance (BLIP) in tens of seconds for broadband infrared observations with Cryoscope. In general, the HELLSTAR requirements are conservative for Cryoscope. For example, the read noise requirement is approximately 30% less than the that required for Cryoscope. The dark current is two orders of magnitude lower than the requirement for Cryoscope. Due to the coldness of the telescope, Cryoscope with HELLSTAR is highly competitive with much larger telescopes. It would produce SNR of approximately 2/3 that of the Hubble Space telescope in the K-band for a 23rd magnitude star in one hour. It even competes with the Keck telescopes that have one hundred times the collecting area and yet only generate an SNR of approximately three times that of HELLSTAR on Cryoscope.

5. CONCLUSIONS

The SATIN detector development program produced devices having performance suitable for astrophysics programs. The final fabricated and tested devices represent the culmination of efforts by RIT and RVS to develop a focal plane design platform based on HgCdTe deposited on silicon wafers. With this success, we now anticipate a greater collaboration, including SCI, to develop HELLSTAR, in particular for an application using a telescope at the South Pole, which is being developed by Kasliwal and Smith of Caltech. The HELLSTAR detector will easily meet the requirements for that telescope and yield SNR that is competitive with the Hubble Space telescope and even the largest telescopes on the ground in the K-band.

5.1 Acknowledgments

5.2 References

[1] G. L. Hansen, J. L. Schmit and T. N. Casselman, "Energy gap versus alloy composition and temperature in Hg1−xCdxTe," *J. Appl. Phys.,* vol. 53, no. 10, p. 7099, 1982.

[2] P. Jerram and J. Beletic, "Teledyne's high performance infrared detectors for Space missions," in *International Conference on Space Optics — ICSO 2018*, Bellingham, 2019.

[3] K. Jóźwikowski, A. Jóźwikowska, M. Kopytko, A. Rogalski and L. R. Jaroszewicz, "Simplified model of dislocations as a SRH recombination channel in the HgCdTe heterostructures," *Infrared Physics and Technology,* vol. 55, no. 1, pp. 98-107, 2012.

[4] R. E. Bornfreund, P. J. Love, A. W. Hoffman, K. J. Ando, E. Corrales, W. D. Ritchie, N. J. Therrien, J. P. Rosbeck, A. Buell, J. Peterson, J. Franklin, M. Vilela, J. Bangs, S. M. Johnson and W. Radford, "Large Format Short-wave HgCdTe Detectors and Focal Plane Arrays," in *Proc. of Military Sensing Symposium*, 2005.

[5] B. Starr, L. Mears, C. Fulk, J. Getty, E. Beuville, R. Boe, C. Tracy, E. Corrales, S. Kilcoyne, J. Vampola, J. Drab, R. Peralta and C. Doyle, "RVS large format arrays for astronomy," in *Proc. of SPIE High Energy, Optical, and Infrared Detectors for Astronomy VII*, Edinburgh, United Kingdom, 2016.

[6] B. J. Hanold, D. F. Figer, J. Lee, K. Kolb, I. Marcuson, E. Corrales, J. Getty and L. Mears, "Large format MBE HgCdTe on silicon detector development for astronomy," in *Proc. of SPIE Infrared Sensors, Devices, and Applications V*, San Diego, 2015.

[7] D. Figer, J. Lee, E. Corrales, J. Getty and L. Mears, "HgCdTe detectors grown on silicon substrates for observational astronomy," in *High Energy, Optical, and Infrared Detectors for Astronomy VIII*, Austin, 2018.

[8] R. Smith and M. Kasliwal, "Cryoscope: A technology pathfinder for time domain astronomy in the NIR," in *Scientific Research Program Astronomy & Astrophysics from Antarctica, September 8-10 Virtual Workshop*, Madison, 2021.

[9] I. S. McLean, Ed., Infrared Astronomy with Arrays: The Next Generation, Series: Astrophysics and Space Science Library, vol. 190, Springer, 1994.

[10] J. R. Janesick, Scientific Charge-coupled Devices, Bellingham, WA: SPIE Publications, 2001.

[11] D. Minniti, P. Lucas, J. Emerson, R. Saito, M. Hempel, P. Pietrukowicz, A. Ahumada, M. Alonso, J. Alonso-García, J. Arias, R. Bandyopadhyay, R. Barbá, B. Barbuy, L. Bedin, E. Bica, J. Borissova, L. Bronfman, G. Carraro, M. Catelan and M. Zoccali, "VISTA Variables in the Via Lactea (VVV): The public ESO near-IR variability survey of the Milky Way," *New Astronomy,* vol. 15, no. 5, pp. 433-443, 2010.

[12] E. L. Wright, P. R. M. Eisenhardt, A. K. Mainzer, M. E. Ressler, R. M. Cutri, T. Jarrett, J. D. Kirkpatrick, D. Padgett, R. S. McMillan, M. Skrutskie, S. A. Stanford, M. Cohen, R. G. Walker, J. C. Mather, D. Leisawitz, T. N. Gautier III, I. McLean, D. Benford, C. J. Lonsdale, A. Blain, B. Mendez, W. R. Irace, V. Duval, F. Liu, D. Royer, I. Heinrichsen, J. Howard, M. Shannon, M. Kendall, A. L. Walsh, M. Larsen, J. G. Cardon, S. Schick, M. Schwalm, M. Abid,

B. Fabinsky, L. Naes and C.-W. Tsai, "The Wide-field Infrared Survey Explorer (WISE): Mission Description and Initial On-orbit Performance," *The Astronomical Journal,* vol. 140, no. 6, pp. 1868-1881, 2010.

[13] P. Capper, J. Garland, S. Kasap and A. Willoughby, Eds., Mercury Cadmium Telluride: Growth, Properties and Applications, Chichester, United Kingdom: John Wiley and Sons Ltd., 2010.

[14] M. Brown, M. Schubnel and G. Tarlé, "Correlated Noise and Gain in Unfilled and Epoxy-Underfilled Hybridized HgCdTe Detectors," *Astronomical Society of the Pacific,* vol. 118, no. 848, pp. 1443-1447, 2006.

[15] R. A. Lundquist, V. Balzano, P. Davila, M. P. Drury, J. L. Dunn, S. D. Glazer, M. A. Greenhouse, E. Greville, G. Henegar, E. L. Johnson, J. C. McCloskey, R. G. Ohl, R. A. Rashford, G. C. Hobbs, S. Lambros, D. McGuffey and M. F. Voyton, "Status of the James Webb Space Telescope Integrated Science," in *Proc. of SPIE Space Telescopes and Instrumentation 2012: Optical, Infrared, and Millimeter Wave*, Amsterdam, Netherlands, 2012.

[16] J. W. Beletic, R. Blank, D. Gulbransen, D. Lee, M. Loose, E. C. Piquette, T. Sprafke, W. E. Tennant, M. Zandian and J. Zino, "Teledyne Imaging Sensors: infrared imaging technologies for astronomy and civil space," in *Proc. of SPIE High Energy, Optical, and Infrared Detectors for Astronomy III*, Marseille, France, 2008.

[17] R. M. Smith, M. Zavodny, G. Rahmer and M. Bonati, "A theory for image persistence in HgCdTe photodiodes," in *Proc. of SPIE High Energy, Optical, and Infrared Detectors for Astronomy III*, Marseille, France, 2008.

[18] " Physics of the Cosmos Program Annual Technology Report," National Aeronautics and Space Administration, 2012.